Robotica: (2021) volume 39, pp. 1328–1343. © The Author(s), 2021. Published by Cambridge University Press.
doi:10.1017/S0263574720001204

A Mathematical Model Including Mechanical Structure, Hydraulic and Control of LHDS

Guoliang Ma†, Kaixian Ba‡*, Zhiwu Han†, Zhengguo Jin¶, Bin Yu¶ and Xiangdong Kong¶

†*The Key Laboratory of Bionic Engineering of Ministry of Education, Jilin University, Changchun, China*
E-mails: mgl@stumail.ysu.edu.cn, zwhan@jlu.edu.cn
‡*School of Mechanical Engineering, Hebei University of Technology, Tianjing, China*
¶*School of Mechanical Engineering, Yanshan University, Qinhuangdao, China*
E-mails: jzg@stumail.ysu.edu.cn, yb@ysu.edu.cn, xdkong@ysu.edu.cn

(Accepted November 24, 2020. First published online: January 20, 2021)

SUMMARY
In this paper, mathematical models of kinematics, statics and inverse dynamics are derived firstly according to the mechanical structure of leg hydraulic drive system (LHDS). Then, all the above models are integrated with MATLAB/Simulink to build the LHDS simulation model, the model not only considers influence of leg dynamic characteristics on hydraulic system but also takes into account nonlinearity, variable load characteristics and other common problems brought by hydraulic system, and solves compatibility and operation time which brought by using multiple software simultaneously. The experimental results show the simulation model built in this paper can accurately express characteristics of the system.

KEYWORDS: Leg hydraulic drive system (LHDS); Kinematics; Dynamics; Position-based impedance control; Simulation model.

1. Introduction

Mobile robots generally include wheeled robots,[1] tracked robots[2] and legged robots.[3] Compared with wheeled robots and tracked robots, legged robots are more adaptable to unknown environments and have broad application prospects.[4] In particular, its combination with compliance control can effectively alleviate the external rigid impact. As a commonly used active compliance control method for legged robots, impedance control can be divided into two common forms: position-based impedance control (i.e., impedance control with position control inner loop) and force-based impedance control (i.e., impedance control with force control inner loop). At present, many scholars have done some research on position impedance control, such as a novel Cartesian space impedance control,[5] neural networks impedance control[6] and joint position-based impedance control.[7] There have also been many scholars research on force-based impedance control such as force-based variable impedance learning,[8] adaptive impedance control,[9] invariance control[10] and impedance-based force control.[11] Compared with the position-based impedance control, the force-based impedance control has faster response speed and robustness, but the position-based impedance control has higher accuracy than the force-based impedance control. Therefore, position-based impedance control is taken as the research object in this paper. Impedance control is not only applied in electric-driven robots such

* Corresponding author. E-mail: bkx@ysu.edu.cn

as Scara,[12] Thevenin,[13] Stewart,[14] rehabilitation robot,[15] Tekken,[16] Scout,[17] KOLT[18] and Cheetah,[19] but as the hydraulic robot becomes more popular, it is also applied in robots such as Bigdog,[20] HyQ,[21] Scalf-1,[22] LWR robot[23] and StarlETH,[24] LS3,[25] JINPOONG,[26] Atlas.[27]

Due to the complex structure of the robot, adopting traditional design and manufacturing methods cannot shorten the design cycle and save the cost. Virtual prototyping technology takes the kinematics, dynamics and control theory of the mechanical system as the core, combines with mature computer technology and graphic-based user interface technology and provides a new design method. By using system simulation software, the motion and force under various working conditions are simulated and analyzed, and different designs are simulated and tested. The whole system can be constantly improved, which can shorten the development cycle, reduce the cost and improve the product quality.[28,29] Therefore, as soon as this technology emerged, it attracted the attention of scholars from all over the world, and they introduced virtual prototyping technology into robot research. Lin Bi[30] used Solidworks and ADAMS to simulate and analyze the dynamics of the amphibious robot and obtained the rotation angle, angular velocity, angular acceleration and torque of each joint, which verified the correctness of Lagrange dynamic equation. However, MATLAB/Simulink cannot be used to optimize the control method. Yang Shanguo[31] built the virtual prototype of two-degree-of-freedom (DOF) hybrid-driven planar parallel manipulator by Pro/E and integrated the model into MATLAB/Simulink to make the virtual model run along the expected trajectory, which verified the effectiveness and practicability of the virtual prototype model. L.F.P. Oliveira[32] used Solidworks to establish the three-dimensional virtual prototype model of the bionic hexapod robot and the contact model between the foot and the ground. The simulation was carried out in MATLAB/SimMechanics to obtain the simulation curves of the joint position and contact force of the robot, which provided a certain reference for the structure and motion control method of hexapod robot; C.A.G. Gutiérrez[33] introduced the kinematics analysis of a five-DOF robot. The model of the robot arm was simulated by MATLAB/Simulink to verify the accuracy of the robot position and applied to robot teaching; He Bin[34] used UG, ADAMS and ANSYS software to carry out cooperative simulation. After establishing the kinematics model of manipulator based on D-H method, the kinematics simulation and numerical simulation of the virtual model were carried out. In addition, the forward and inverse kinematics simulation were completed quickly by using MATLAB. The relationship between the forward motion and the reverse motion of the manipulator was obtained. Finally, the kinematics experiment was carried out on the physical prototype of the manipulator, which proved the accuracy of the kinematics calculation and the rationality of the design based on the rigid-flexible coupling virtual prototype; Xie Hualong[35] et al. studied a wearable biped robot and carried out continuous walking simulation based on Pro/E, ADAMS and MATLAB/Simulink, which verified the feasibility of joint simulation; Lan Zhi[36] built the virtual prototype and co-simulation platform based on ADAMS and MATLAB/Simulink software, simulated the kinematics, dynamics and control methods of the upper limb rehabilitation robot, obtained the kinematics parameters of each joint and determined the parameters of the controller.

In the above references, references[30–33] use a software to build a simulation model for research. References[34–36] use multi-software co-simulation for research. However, most of the simulation studies in the above references only focus on the nature properties of robot mechanical structure or the characteristics of a certain aspect of robot control system, such as robot dynamics analysis,[30,36] robot kinematics analysis,[31–36] robot mechanical structure optimization[31,34] and robot motion control method research.[32,35,36] Actually, leg hydraulic drive system (LHDS) is mainly composed of control system, hydraulic system and mechanical structure, if we adopt the method of multiple software co-simulation in the above references, due to the different simulation framework for research, which will result in some problems, such as complicated operations, poor fit and slow running speed. So how to build a simulation model that contains mechanical structure, hydraulic drive system and control system, which can accurately represent the characteristics of the system, and reflect the coupling relationship between mechanical structure, hydraulic drive system and control system by only using one software, and can also really simulate motion of LHDS. It can lay a foundation for related experimental research and practical application and has important significance for shortening the development cycle and reducing the research cost.

LHDS is the basis for the research of legged robots; its performance directly determines the control performance of the entire robot. The joint actuator of LHDS is the second generation hydraulic

https://doi.org/10.1017/S0263574720001204 Published online by Cambridge University Press

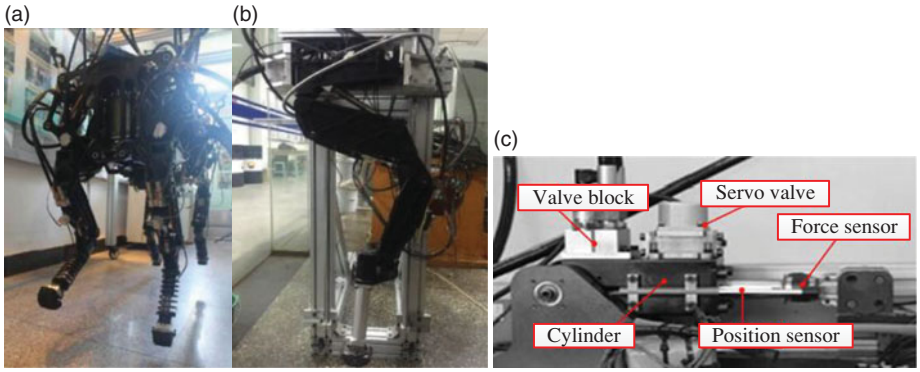

Fig. 1. The quadruped robot prototype, LHDS and hydraulic drive unit (HDU-2nd) performance test platform. (a) Quadruped robot prototype; (b) LHDS; (c) HDU-2nd.

driving unit (HDU-2nd). As the core component of LHDS, the accuracy of its position control system model will directly affect the accuracy of the overall simulation model. In the author's previous researches, a mathematical model for nonlinear position control has been built for the first generation hydraulic driving unit (HDU-1st) with a valve-controlled symmetrical cylinder structure, which includes servo valve dynamic characteristics, pressure-flow nonlinearity and initial displacement and friction nonlinearity of the servo cylinder piston. And the sensitivity analysis theory is applied to quantitatively analyze the influence degree of various parameters changes on system control performance in HDU-1st position control system. The HDU-2nd applied in the LHDS adopts the asymmetric cylinder structure for improving load capacity. The structure size and component type are very different from the HDU-1st. The author's previous research work on HDU-1st can provide a reference for the construction of the mathematical model of the HDU-2nd position control system.

2. Mathematical Model of LHDS

2.1. Mathematical model of HDU position-based control system

Figure 1 shows the photos of the quadruped robot prototype; the LHDS uses HDU-2nd with valve-controlled asymmetrical cylinder.

Fig. 2 shows the mathematical model of the HDU-2nd position control system, in which Fig. 2(b) is the simplified Fig. 2(a). The derivation in detail and performance analysis are presented in Appendix.

In Fig. 2, X_r is input position, X_p is position tested by position sensor, E_p is error between the desired position and the actual position, ΔX_p is output position , K_X is position sensor gain, nK_{PID} is PID controller gain, U_g is input voltage for servo amplifier board, K_a is the servo valve amplifier gain, K_{xv} is servo valve gain, $K_{axv} = K_a K_{xv}$, ω is natural frequency of servo valve, ζ is damping ratio of servo valve, $K_d = C_d W\sqrt{2/\rho}$ (K_d is defined as conversion coefficient in this paper), X_v is servo valve spool displacement, p_s is system supply oil pressure, p_1 is inlet cavity pressure of servo cylinder, p_2 is outlet cavity pressure of servo cylinder, p_0 is system return oil pressure, Q_1 is inlet oil flow, Q_2 is outlet oil flow, C_{ip} is internal leakage coefficient of servo cylinder, C_{ep} is external leakage coefficient of servo cylinder, L is total length of piston rod, L_0 is initial length of piston rod, V_{g1} is volume of input oil pipe, V_{g2} is volume of output oil pipe, A_{p1} is inlet cavity effective piston area of servo cylinder, A_{p2} is outlet cavity effective piston area of servo cylinder, F_{f1} is internal Coulomb friction, F_{f2} is outer Coulomb friction, F_L is load force, m_{t1} is conversion mass, m_{t2} is load mass, B_{p1} is damping coefficient, B_{p2} is damping coefficient of load, $G_f(s)$ is the transfer function applied to the system by the disturbance force, and both $G_1(s)$ and $G_2(s)$ are the transfer functions of the system.

2.2. Kinematics and statics analysis of LHDS

During the motion, LHDS needs to obtain the position and force of the foot end in real time to realize the motion control of LHDS. As shown in Fig. 1(c), a position sensor and a force sensor are mounted on both the knee and ankle joints. Position sensor is used to detect elongation of HDU-2nd; force sensor is used to detect output force of HDU-2nd. Through the structural relation of LHDS,

https://doi.org/10.1017/S0263574720001204 Published online by Cambridge University Press

Table I. D-H parameters of LHDS mechanical structure.

Connecting rod	a_{i-1}	η_{i-1}	d_i	θ_i
1	0	0	0	θ_1
2	l_1	0	0	θ_2
3	l_2	0	0	–

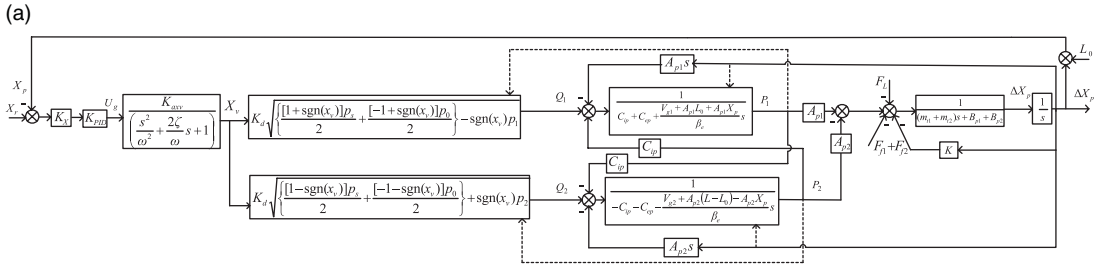

The mathematical model of the HDU-2nd position control system

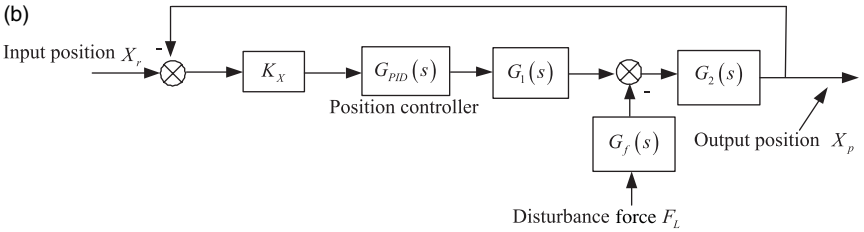

The simplified mathematical model of the HDU-2nd position control system

Fig. 2. Block diagram of HDU-2nd position control system. (a) The mathematical model of the HDU-2nd position control system. (b) The simplified mathematical model of the HDU-2nd position control system.

the relation between the position and output force of the foot and the elongation and output force of HDU-2nd applied to each joint can be obtained.

Due to complex mechanical structure of LHDS, the picture shown in Fig. 1(b) is simplified to picture in Fig. 3 for convenient analysis and calculation. In Fig. 3, root joint O is the origin of coordinates, horizontal right is the positive direction of x_0 axis and the vertical direction is the positive direction of y_0 axis. OD is the length of thigh component and set as l_1. DF is the length of the calf component and set as l_2. The positive rotation angle between thigh and x_0 axis is the rotation angle θ_1 of the knee joint; the rotation angle in the direction of the extension line between the leg and the thigh is the rotation angle θ_2 of the ankle joint. The counterclockwise is the positive direction of the joint rotation angle. AB and CE are the total length of HDU-2nd on the knee and ankle joint, respectively, and the drive torque of the knee joint is τ_1, T the drive torque of the ankle joint is τ_2 and the force of F point on the foot end is $\boldsymbol{F} = (f_x, f_y)$.

D-H parameters of LHDS mechanical structure are shown in Table I.

In Table I, a_{i-1} is defined as the distance measured from z_{i-1} to z_i along x_{i-1}. η_{i-1} is defined as the angle from z_{i-1} to z_i around x_{i-1}. d_i is defined as the distance measured from x_{i-1} to x_i along z_i.θ_i is defined as the angle from x_{i-1} to x_i around z_i.

In D-H coordinate system as shown in Fig. 3(a), the position relation can be expressed by the transformation general formula of the connected rod ${}^{i-1}_{i}T$

$$
{}^{i-1}_{i}T = \begin{bmatrix} \cos\theta_i & -\sin\theta_i & 0 & a_{i-1} \\ \sin\theta_i \cos\eta_{i-1} & \cos\theta_i \cos\eta_{i-1} & -\sin\eta_{i-1} & -d_i \sin\eta_{i-1} \\ \sin\theta_i \sin\eta_{i-1} & \cos\theta_i \sin\eta_{i-1} & \cos\eta_{i-1} & d_i \cos\eta_{i-1} \\ 0 & 0 & 0 & 1 \end{bmatrix} \tag{1}
$$

https://doi.org/10.1017/S0263574720001204 Published online by Cambridge University Press

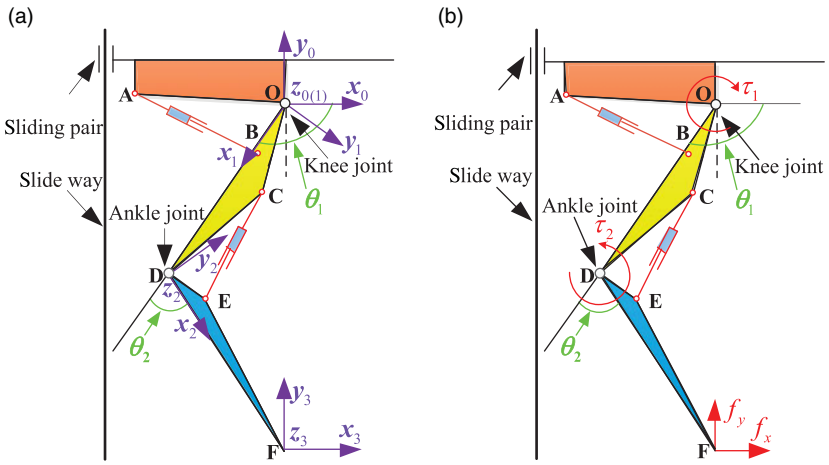

Fig. 3. (a) Diagram of LHDS kinematics model; (b) diagram of LHDS statics model.

According to Table I, and combining with Eq. (1), the transformation matrix between adjacent links is obtained.

$$ {}^{0}_{1}T = \begin{bmatrix} \cos\theta_1 & -\sin\theta_1 & 0 & 0 \\ \sin\theta_1 & \cos\theta_1 & 0 & 0 \\ 0 & 0 & 1 & 0 \\ 0 & 0 & 0 & 1 \end{bmatrix} \tag{2} $$

$$ {}^{1}_{2}T = \begin{bmatrix} \cos\theta_2 & -\sin\theta_2 & 0 & l_1 \\ \sin\theta_2 & \cos\theta_2 & 0 & 0 \\ 0 & 0 & 1 & 0 \\ 0 & 0 & 0 & 1 \end{bmatrix} \tag{3} $$

$$ {}^{2}_{3}T = \begin{bmatrix} \cos\theta_3 & -\sin\theta_3 & 0 & l_2 \\ \sin\theta_3 & \cos\theta_3 & 0 & 0 \\ 0 & 0 & 1 & 0 \\ 0 & 0 & 0 & 1 \end{bmatrix} \tag{4} $$

${}^{0}_{3}T$ can be obtained by multiplying Eqs. (2), (3) and (4), respectively.

$$ {}^{0}_{3}T = {}^{0}_{1}T\,{}^{1}_{2}T\,{}^{2}_{3}T = \begin{bmatrix} \cos(\theta_1+\theta_2+\theta_3) & -\sin(\theta_1+\theta_2+\theta_3) & 0 & l_1\cos\theta_1 + l_2\cos(\theta_1+\theta_2) \\ \sin(\theta_1+\theta_2+\theta_3) & \cos(\theta_1+\theta_2+\theta_3) & 0 & l_1\sin\theta_1 + l_2\sin(\theta_1+\theta_2) \\ 0 & 0 & 1 & 0 \\ 0 & 0 & 0 & 1 \end{bmatrix} \tag{5} $$

The positive kinematics solution can be obtained from Eq. (5).

$$ \begin{cases} x = l_1\cos\theta_1 + l_2\cos(\theta_1+\theta_2) \\ y = l_1\sin\theta_1 + l_2\sin(\theta_1+\theta_2) \end{cases} \tag{6} $$

If angle of the knee joint and ankle joint and length of the connected rod are known, then according to Eq. (6), the position relation of the foot end relative to the root joint O can be obtained.

https://doi.org/10.1017/S0263574720001204 Published online by Cambridge University Press

The inverse kinematic solution can be obtained by combining Eq. (6), that is, when the foot end position of LHDS is independent variable, the joint of knee and ankle can be expressed as follows:

$$\begin{cases} \theta_1 = \arctan2(y, x) - \arccos\left(\dfrac{x^2 + y^2 + l_1^2 - l_2^2}{2l_1\sqrt{x^2 + y^2}}\right) \\ \theta_2 = \arccos\left(\dfrac{x^2 + y^2 + l_1^2 - l_2^2}{2l_1 l_2}\right) \end{cases} \tag{7}$$

According to the virtual work principle, the sum of the work done by the virtual position of each joint is equal to the sum of the work done by the end-effector, so the relation of the statics inverse solution can be expressed as follows:

$$\boldsymbol{\tau} = \boldsymbol{J}^{\mathrm{T}}(\boldsymbol{q})\,\boldsymbol{F} \tag{8}$$

where $J^{\mathrm{T}}(\boldsymbol{q})$ is the force Jacobean of LHDS, that is, the linear relationship between the foot end force and joint torque under static equilibrium state can be expressed as follows:

$$J^{\mathrm{T}}(\boldsymbol{q}) = \begin{bmatrix} \dfrac{\partial x}{\partial \theta_1} & \dfrac{\partial y}{\partial \theta_1} \\ \dfrac{\partial x}{\partial \theta_2} & \dfrac{y}{\partial \theta_2} \end{bmatrix} = \begin{bmatrix} -l_1 \sin\theta_1 - l_2 \sin(\theta_1 + \theta_2) & l_1 \cos\theta_1 + l_2 \cos(\theta_1 + \theta_2) \\ -l_2 \sin(\theta_1 + \theta_2) & l_2 \cos(\theta_1 + \theta_2) \end{bmatrix} \tag{9}$$

Prescribed positive direction of the joint torque vector is counterclockwise, so the joint torque vector $\boldsymbol{\tau}$ can be expressed as follows:

$$\boldsymbol{\tau} = [\tau_1, \tau_2]^{\mathrm{T}} \tag{10}$$

Inserting Eqs. (9) and (10) into Eq. (8), the inverse static solution can be obtained, that is, when the foot end force is independent variable, and output torque of knee and ankle joint can be expressed as follows:

$$\begin{cases} \tau_1 = -f_x\,(l_1 \sin\theta_1 + l_2 \sin(\theta_1 + \theta_2)) + f_y\,(l_1 \cos\theta_1 + l_2 \cos(\theta_1 + \theta_2)) \\ \tau_2 = -f_x l_2 \sin(\theta_1 + \theta_2) + f_y l_2 \cos(\theta_1 + \theta_2) \end{cases} \tag{11}$$

Inversing Eq. (8), the positive static solution can be expressed as follows:

$$\boldsymbol{F} = \left[\boldsymbol{J}^{\mathrm{T}}(\boldsymbol{q})\right]^{-1} \boldsymbol{\tau} \tag{12}$$

where

$$\left[J^{\mathrm{T}}(\boldsymbol{q})\right]^{-1} = \frac{1}{l_1 l_2 \sin\theta_2} \begin{bmatrix} l_2 \cos(\theta_1 + \theta_2) & -[l_1 \cos\theta_1 + l_2 \cos(\theta_1 + \theta_2)] \\ l_2 \sin(\theta_1 + \theta_2) & -[l_1 \sin\theta_1 + l_2 \sin(\theta_1 + \theta_2)] \end{bmatrix} \tag{13}$$

Inserting Eq. (13) into Eq. (12), and combining Eq. (10), the positive static solution can be obtained.

$$\begin{cases} f_x = \dfrac{1}{l_1 l_2 \sin\theta_2}\,[\tau_1 l_2 \cos(\theta_1 + \theta_2 - \tau_2\,[l_1 \cos\theta_1 + l_2 \cos(\theta_1 + \theta_2)]] \\ f_y = \frac{1}{l_1 l_2 \sin\theta_2}\,[\tau_1 l_2 \sin(\theta_1 + \theta_2) - \tau_2\,[l_1 \sin\theta_1 + l_2 \sin(\theta_1 + \theta_2)]] \end{cases} \tag{14}$$

2.3. Inverse dynamics of LHDS modeling

To reduce the effect of dynamics characteristic on the position-based impedance motion control. The paper solves the inverse dynamics by the measured value of the position sensor of LHDS; the compensation of the gravity and inertia force in current motion state is calculated. Therefore, the accuracy of the position-based impedance motion control system can be improved.

Because center-of-mass of HDU-2nd has a little change during the motion, for convenient calculation and modeling, change of center-of-mass can be ignored. Therefore, the picture shown in Fig. 1(b) can be simplified to Fig. 4.

https://doi.org/10.1017/S0263574720001204 Published online by Cambridge University Press

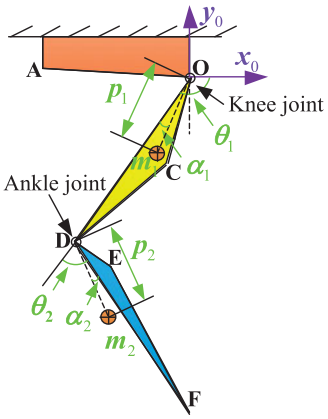

Fig. 4. Simplified diagram of LHDS dynamics model.

In Fig. 4, α_1 and α_2 are the deviation angles of the center-of-mass of component OD and component DF relative to the straight line OD and the straight line DF, respectively. p_1 and p_2 are the distance of the center-of-mass of component OD and component DF relative to the point O and the point D.

According to geometrical relationship in Fig. 4, center-of-mass coordinate of components OD $m_1(x_1, y_1)$can be obtained.

$$\begin{cases} x_1 = p_1 \cos(\theta_1 + \alpha_1) \\ y_1 = p_1 \sin(\theta_1 + \alpha_1) \end{cases} \tag{15}$$

When component OD rotates around z_1 axis, the rotational inertia is J_1, the kinetic energy E_{k1} of component OD can be obtained

$$E_{k1} = \frac{1}{2} m_1 (p_1 \theta_1)^2 + \frac{1}{2} J_1 \dot{\theta}_1^2 \tag{16}$$

The potential energy E_{m1} can be expressed

$$E_{m1} = m_1 g p_1 \sin(\theta_1 + \alpha_1) \tag{17}$$

where g is the gravitational acceleration.

According to geometrical relationship in Fig. 4, center-of-mass coordinate of components OD $m_2(x_2, y_2)$ can be obtained

$$\begin{cases} x_2 = l_1 \cos\theta_1 + p_2 \cos(\theta_1 + \theta_2 + \alpha_2) \\ y_2 = l_1 \sin\theta_1 + p_2 \sin(\theta_1 + \theta_2 + \alpha_2) \end{cases} \tag{18}$$

When component DF rotates around z_2 axis, the rotational inertia is J_2, the kinetic energy E_{k2} of component DF can be obtained

$$E_{k2} = \frac{1}{2} m_2 l_1^2 \dot{\theta}_1^2 + \frac{1}{2} m_2 p_2^2 (\theta_1 + \dot{\theta}_2)^2 + m_2 l_1 p_2 (\dot{\theta}_1^2 + \dot{\theta}_1 \dot{\theta}_2) \cos(\theta_2 + \infty_2) + \frac{1}{2} J_2 (\dot{\theta}_1 + \dot{\theta}_2) \tag{19}$$

The potential energy E_{m2} can be expressed

$$E_{m2} = m_2 g l_1 \sin\theta_1 + m_2 g p_2 \sin(\theta_1 + \theta_2 + \alpha_2) \tag{20}$$

The Lagrangian kinetic equation can be obtained

$$\frac{d}{dt}\left(\frac{\partial L_{ag}}{\partial \dot{q}_j}\right) - \frac{\partial L_{ag}}{\partial q_j} = Q_j \tag{21}$$

https://doi.org/10.1017/S0263574720001204 Published online by Cambridge University Press

where q_j is the generalized coordinates, Q_j is the generalized force corresponding to the generalized coordinates and L_{ag} is the Lagrangian function.

$$L_{ag} = E_k - E_m \tag{22}$$

The Lagrangian function is used to solve the dynamic equation. Inserting Eq. (16), (17), (19), (20) and (22), the torque of the knee joint and ankle joint can be obtained during different motion; the mathematical relation of the inverse dynamics of LHDS can be solved as follows:

$$\begin{cases} \tau_1 = D_{11}\ddot{\theta}_1 + D_{12}\ddot{\theta}_2 + D_{112}\dot{\theta}_1\dot{\theta}_2 + D_{122}\dot{\theta}_2^2 + D_1 \\ \tau_2 = D_{21}\ddot{\theta}_1 + D_{22}\ddot{\theta}_2 + D_{211}\dot{\theta}_1^2 + D_2 \end{cases} \tag{23}$$

where

$$\begin{cases} D_{11} = m_1 p_1^2 + m_2 p_2^2 + m_2 l_1^2 + 2 \cdot m_2 l_1 p_2 \cos(\theta_2 + \alpha_2) + J_1 + J_2] \\ D_{12} = m_2 p_2^2 + m_2 l_1 p_2 \cos(\theta_2 + \alpha_2) + J_2 \\ D_{112} = -2 m_2 l_1 p_2 \sin(\theta_2 + \alpha_2) \\ D_{122} = -m_2 l_1 p_2 \sin(\theta_2 + \alpha_2) \\ D_1 = m_1 g p_1 \cos(\theta_1 + \alpha_1) + m_2 g l_1 \cos\theta_1 + m_2 g p_2 \cos(\theta_1 + \theta_2 + \alpha_2) \end{cases} \tag{24}$$

$$\begin{cases} D_{21} = m_2 p_2^2 + m_2 l_1 p_2 \cos(\theta_2 + \alpha_2) + J_1 \\ D_{22} = m_2 p_2^2 + J_1 \\ D_{211} = m_2 l_1 p_2 \sin(\theta_2 + \alpha_2) \\ D_2 = m_2 g p_2 \cos(\theta_1 + \theta_2 + \alpha_2) \end{cases} \tag{25}$$

It can be seen from kinematics model in Fig. 3 that the joint angle displacement θ_1 and θ_2 are related to two cylinders' displacement. The terms that contain $\ddot{\theta}_1$ and $\ddot{\theta}_2$ are the joint inertia torque term caused by the acceleration. The terms that contain $\dot{\theta}_1$ and $\dot{\theta}_2$ are the coupling torque term caused by the centripetal force. The terms that contain $\dot{\theta}_1\dot{\theta}_2$ is the coupling torque term caused by the Coriolis force. The terms that contain θ_1 and θ_2 are the joint torque term caused by the Coriolis force.

3. LHDS Simulation Model of Position-Based Impedance Motion Control

This section based on kinematics, statics and inverse dynamics of mechanical structure and mathematical model of HDU-2nd position-based control system is derived in second section, a simulation model of LHDS that contains mechanical structure, hydraulic drive system and control system is built and the principle of LHDS position-based impedance motion control is introduced.

Combining the mathematical models of kinematics, statics and inverse dynamics derived and the mathematical model of HDU-2nd position control system in second section, the principle of the position-based impedance motion control built by MATLAB/Simulink is shown in Fig. 5.

It can be seen from Fig. 5, position-based impedance motion control of LHDS can be carried out in three steps.

Firstly, through impedance control outer loop, the disturbance signal of the foot end measured by the force sensor can be obtained.

When the foot end is disturbed, the force sensor applied to the knee joint and ankle joint can detect force signal. The force signal consists of two parts. First part is the force signal component acting on the foot end of the disturbance force detected by the force sensor. Second part is the force signal component of gravity and inertia force of the mechanical structure detected by the force sensor, because the force signal of the second part is not generated by the disturbance force acting on the foot end. If the force detected by force sensor is taken as the disturbance force of the impedance control directly, the accuracy of the motion control will be influenced. In order to obtain the disturbance force of the position-based impedance control, it is necessary to combine with inverse dynamics to obtain the force signal of the second part.

Secondly, through impedance control outer loop, the disturbance signal is converted to the input signal of the position control inner loop.

https://doi.org/10.1017/S0263574720001204 Published online by Cambridge University Press

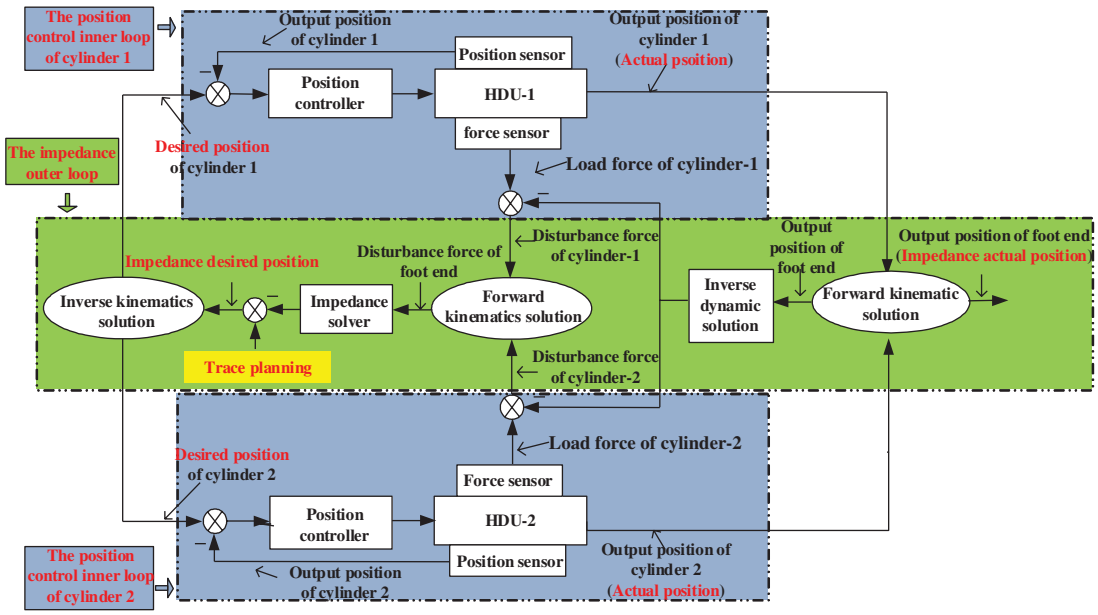

Fig. 5. The principle of the position-based impedance motion control of LHDS.

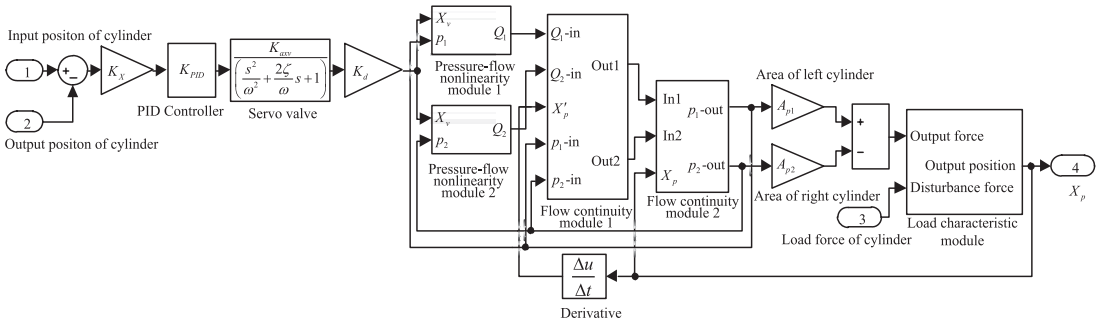

Fig. 6. The simulation model of HDU-2nd position control system.

After the disturbance force acting on HDUs applied to the knee joint and ankle joint is obtained, the disturbance force acting on the foot end can be solved by the statics positive solution. Then, through impedance characteristic solver, the position variation corresponding to the disturbance force signal can be solved. Finally, through kinematics inverse solution, variation of the input signal of the potion control inner loop can be solved.

Lastly, input and output control are realized in position control inner loop.

When the position control inner loop is given an input signal, it is converted to control signal of the control component (servo valve), and then control signal is converted to the output position signal of the actuator (servo cylinder).

In Fig. 5, the blue part is the position control inner loop of HDU-2nd, which is the impedance control core component of LHDS; its accuracy of the position control system model will directly affect the accuracy of the whole simulation model. Then based on the block diagram of HDU-2nd position control system shown in Fig. 2, the simulation model of HDU-2nd position control system is built on MATLAB-Simulink simulation platform, which is shown as Fig. 6.

The simulation model of HDU-2nd position control system shown in Fig. 6 is used to simulate the position control performance of HDU-2nd in the actual motion. The model includes the servo valve dynamic characteristics, the pressure-flow nonlinearity, the initial position of the servo cylinder piston and the friction nonlinearity, which makes the position control system built in this paper more close to the real system. In Fig. 6, there are three input modules: modules 1, 2, 3 and one output module: module 4. The input of module 1 is the desired impedance position of cylinder 1 (cylinder 2) shown in Fig. 7, the input of module 2 is the output position of cylinder 1 (cylinder 2) shown in

https://doi.org/10.1017/S0263574720001204 Published online by Cambridge University Press

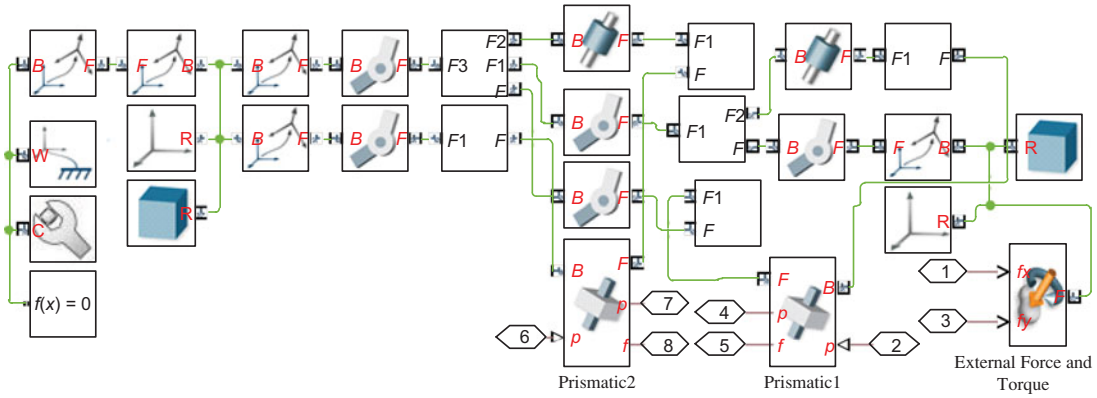

Fig. 7. Simulation model of leg mechanical structure.

Fig. 7 and the input of module 3 is load force of cylinder 1 (cylinder 2) shown in Fig. 7. The output of module 4 is the output position of cylinder 1 (cylinder 2) shown in Fig. 7.

In Fig. 5, the green part is impedance control outer loop, which is built based on the simulation model of mechanical structure of LHDS. Therefore, simulation model of the mechanical structure is built by using SimMechanics in MATLAB. SimMechanics can establish 3D model of the mechanical structure clearly. The advantage of SimMechanics is the analysis of the control system and dynamics simulation of the mechanical system, and the basic kinematics algebraic equations and dynamic differential equations are encapsulated. However, the ability of 3D modeling is weaker than professional CAD software; the assembly file of the leg mechanical structure is exported into an XML file and several STL files by using SimMechanics Link tool of Solidworks software. Then, running the simport command in the MATLAB, MATLAB will automatically read the corresponding XML file and STL files, and automatically built the SimMechanics model of LHDS mechanical structure as shown in Fig. 7.

In Fig. 7, model prismatic is used to connect piston rod and cylinder block and has one input module: module 2 (module 6), and two output modules: modules 4 and 5 (modules 7 and 8). Among them, the input of module 2 (module 6) is the output of module 4 in Fig. 6 (the output position of cylinder 1/cylinder 2), the output of module 4 (module 7) is the input of module 2 in Fig. 6 (the actual position of cylinder 1 (cylinder 2) is measured through the sensing attribute in Prismatic module), the output of module 5 (module 8) is the input of module 3 in Fig. 6 (the load force of cylinder 1 (cylinder 2) is actually measured through the sensing attribute in Prismatic module).

The simulation model of leg mechanical structure shown in Fig. 7 is used to connect the impedance control outer loop and the position control inner loop of HDU-2nd. This model can realize real-time control of foot-end position through the output of module 4 in Fig. 6. The load force of cylinder 1 (cylinder 2) is actually measured through the sensing attribute in Prismatic module and output to module 3 in Fig. 6, which is used to simulate the load force of the position control inner loop. External force and torque module is imposed force to the foot end to simulate the disturbance force of the foot end in the actual motion.

Combining the above analysis, finally, a simulation model of LHDS including mechanical structure, hydraulic drive system and control system is built. After running the simulation program, the 3D model of LHDS can be seen as shown in Fig. 8, through which the motion state of LHDS can be observed.

4. Simulation and Experiment

In this section, the accuracy of the simulation model of LHDS position-based impedance motion control established in this paper is tested. The LHDS experimental platform is shown in Fig. 1(b), and its principle of the hydraulic system is shown in Fig. 9. The HDU-2nd of each joint is controlled independently and uniformly supplied with oil.

Setting the stiffness coefficient of X-axis and Y-axis of LHDS as 10 N/mm, and the damping coefficient as 0.5 Ns/mm.

https://doi.org/10.1017/S0263574720001204 Published online by Cambridge University Press

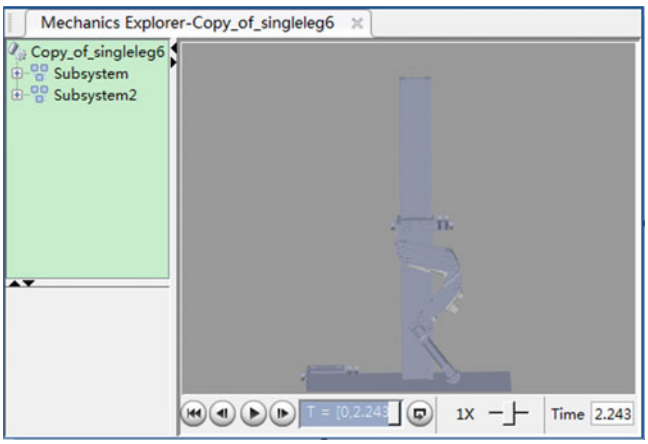

Fig. 8. 3D model of LHDS.

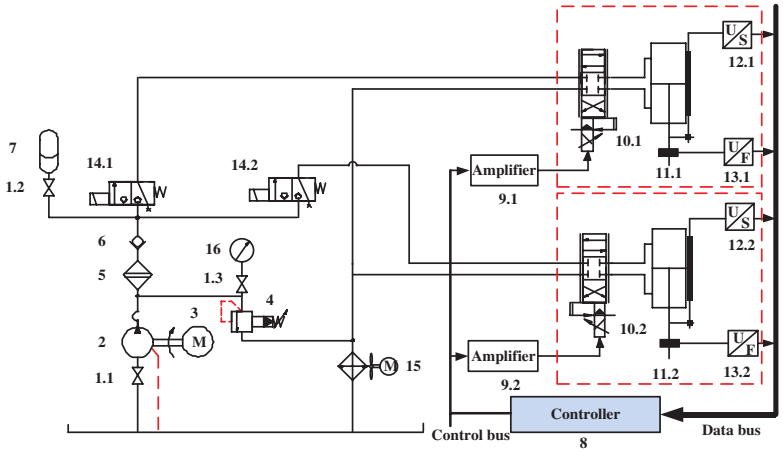

1-stop valve 2-metering pump 3-motor 4-overflow valve 5-high pressure filter 6-check valve 7-accumulator 8-dSPACE controller 9- power amplifier 10-electro-hydraulic servo valve 11-servo cylinder 12-position sensor 13-force sensor 14-magnetic exchange valve 15-air Cooler

Fig. 9. Schematic diagram of hydraulic power system.

Working condition 1:

LHDS is suspended at the initial position ($\theta_1 = -120°$, $\theta_2 = 60°$). In the static state, the random disturbance force is applied to the foot end by hand. The disturbance forces on the X axis and Y axis of the foot end are recorded by the controller, and the measured disturbance force is inputted into the simulation model built in the third section. In this paper, the disturbance force curves, position response curves and the impedance control response curves of the experimental system and simulation model are given as shown in Fig. 10. The impedance desired position is the ratio of the disturbance force acting on the foot end to the desired impedance characteristic, and the impedance actual position is the actual output position of the system.

As can be seen from Fig. 10, the maximum disturbance force in X direction of the foot end near 2 s is 61.45 N, and the corresponding desired, simulated, experimental impedance control responses in X direction are 5.96, 6.18 and 6.61 mm, respectively, The maximum disturbance force in Y direction of the foot end is 134.98 N, and the corresponding desired, simulated, experimental impedance control responses in Y direction are 13.35, 13.42 and 13.52 mm, respectively. The maximum disturbance force in X direction near 6 s is 66.12 N, and the corresponding desired, simulated and experimental impedance control responses in X direction are 6.54, 6.87 and 7.08 mm, respectively. The maximum disturbance force in Y direction is 135.42 N, and the corresponding desired, simulated and experimental impedance control responses in Y direction are 13.54, 13.68 and 13.76 mm, respectively. It can be obtained that both simulation and experiment can achieve good impedance characteristics.

https://doi.org/10.1017/S0263574720001204 Published online by Cambridge University Press

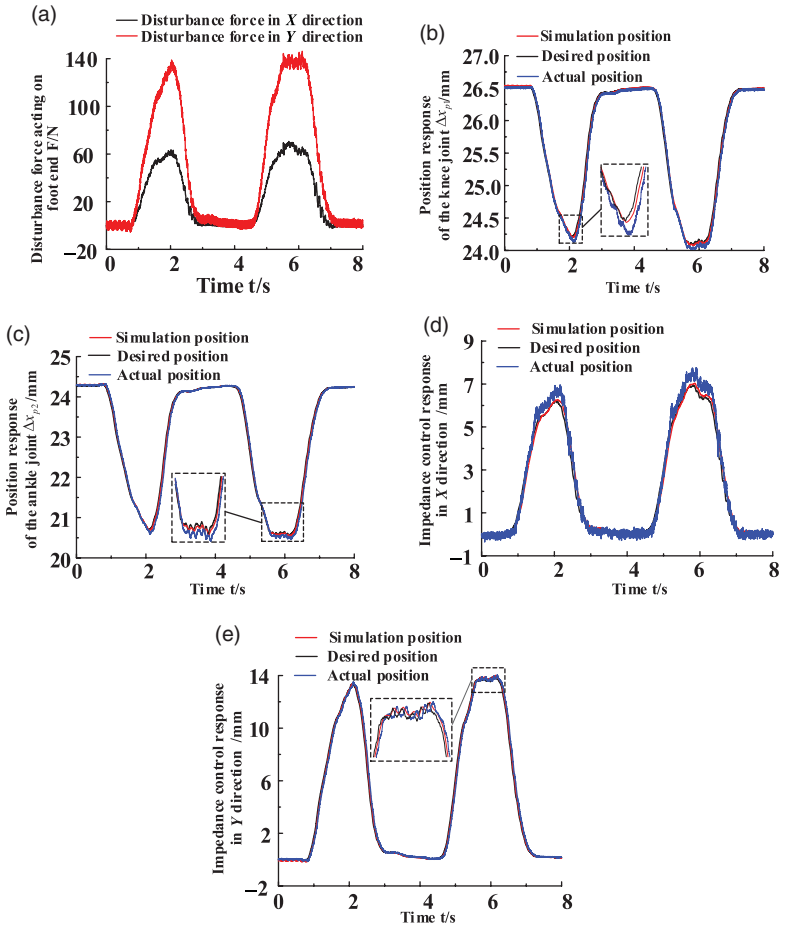

Fig. 10. Motion control response curve of LHDS position-based impedance in static state. (a) Disturbance forces in the X and Y directions of the foot end. (b) Position response curves of the knee joint. (c) Position response curve of the ankle joint. (d) Impedance control response curves in X axis direction of the foot end. (e) Impedance control response curves in Y axis direction of the foot end.

It can be seen from Fig. 10(b)–(c) that the actual and simulated position responses of the HDU-2nd lag behind the desired position, and the position responses at the two maximum disturbance forces exceed the desired position response. When the foot end is at the initial position and subject to random disturbance force in static state, the simulation model built in this paper has a high fitting degree with the experimental system and can accurately present the system characteristics.

Working condition 2:

LHDS is suspended and is made with a circular motion of a frequency of 0.5 Hz and a radius of 10 mm with the initial position as the origin. The disturbance force of the foot end measured in experiment is inputted into the simulation model built in the third section. The relevant simulated and experimental curves are shown in Fig. 11.

As can be seen from Fig. 11, the foot end is not disturbed in the first 2 s, and the simulation model and the experimental system achieve good position tracking in both the X and Y directions. The maximum disturbance force in X direction of the foot end near the 7 s is 64.39 N. At this time, the motion direction of the foot end is opposite to the direction of the force in X direction, and the amplitude is reduced. The corresponding desired, simulated, experimental impedance control responses in X direction are −2.12, −2.76 and −2.47 mm, respectively. The maximum disturbance force in Y direction of the foot end near the 7 s is 132.52N. At this time, the motion direction of the foot end is same to the direction of the force in Y direction, and the amplitude becomes larger. The corresponding desired, simulated, experimental impedance control responses in Y direction are 20.69, 20.39 and 19.94 mm, respectively. The maximum disturbance force in X direction of the foot end near 13.2 s is −36.53 N. At this time, the motion direction of the foot end is same to the direction of the force

https://doi.org/10.1017/S0263574720001204 Published online by Cambridge University Press

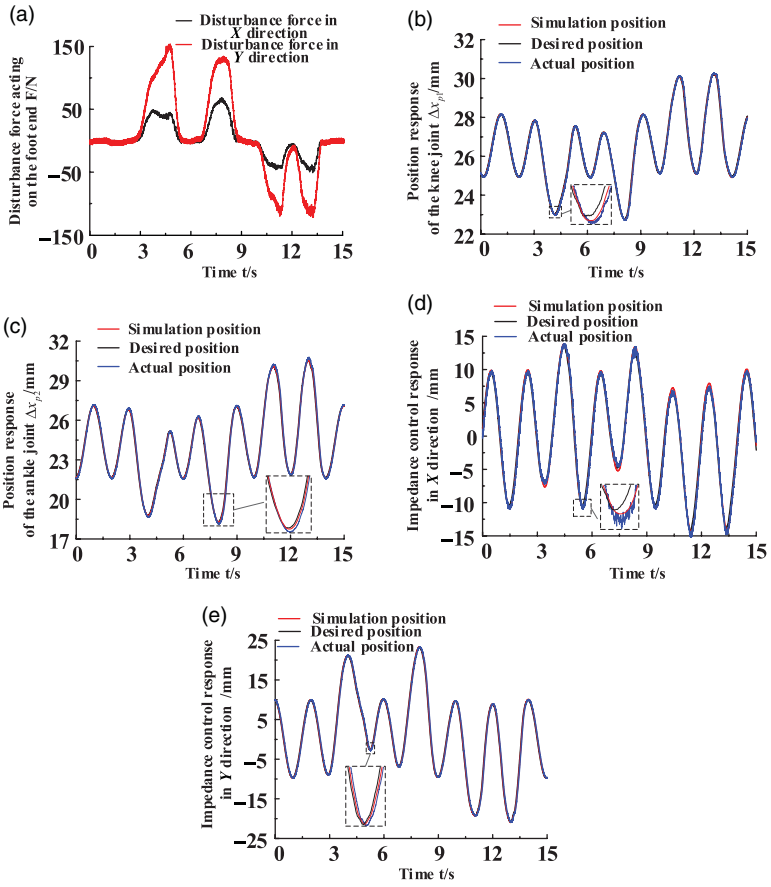

Fig. 11. Motion control response curves of LHDS position-based impedance in motion state. (a) Disturbance forces in *X* and *Y* directions of the foot end. (b) Position response curves of the knee joint. (c) Position response curves of the ankle joint. (d) Impedance control response curves in *X* direction. (e) Impedance control response curves in *Y* direction.

in *Y* direction, the amplitude becomes larger. The corresponding desired, simulated, experimental impedance control responses in *X* direction are −13.58, −13.29 and −13.80 mm, respectively. The maximum disturbance force in *Y* direction of the foot end near the 13.2 s is −109.12N. At this time, the motion direction of the foot end is same to the direction of the force in *X* direction, and the amplitude becomes larger. The corresponding desired, simulated, experimental impedance control responses in *X* direction are −16.23, −17.46 and −17.92 mm, respectively. LHDS is placed in a suspended position and is made with a circular motion of a frequency of 0.5 Hz and a radius of 10 mm with the initial position as the origin. Both the simulation model and the experimental system achieve the desired impedance characteristics while achieve good position following under the effect of the different disturbance forces. The simulation model built in this paper has a high fitting degree with the experiment and can accurately present the system characteristics.

5. Conclusion

In this paper, mathematical models of kinematics, statics and inverse dynamics of LHDS mechanical structure are derived. Based on the derived model, the mathematical model of HDU-2nd position control system and the principle of LHDS position-based impedance motion control, a simulation model of LHDS including mechanical structure, hydraulic drive system and control system is built. By analyzing simulated and experimental results, it is verified that the model built in this paper can accurately represent the system characteristics. Moreover, the mechanical structure, hydraulic drive system and control system of the simulation model are carried out simultaneously under the same simulation framework, which makes the whole simulation model simpler and better compatibility than the joint simulation using multiple software. The research work in this paper can lay a foundation for the related experimental research and practical application of LHDS and can provide a certain

https://doi.org/10.1017/S0263574720001204 Published online by Cambridge University Press

reference for the design, manufacture and optimization of the hydraulic drive legged robot, and for the construction of the simulation model of the mechanical system with complex structure in the future.

Acknowledgment

Research supported by the National Key Research and Development Project [No. 2018YFB2000701], Natural Science Foundation of Hebei Province [No. E2019203021] and the National Natural Science Foundation of China [No. 51905465].

References

1. M. Tavakoli, J. Lourenço, C. Viegas, P. Neto and A. T. Almeida, "The hybrid Omni Climber robot: Wheel based climbing, arm based plane transition, and switchable magnet adhesion", *Mechatronics* **36**, 136–146 (2016).
2. L. Zhang and Y. Qiu, "Design and analysis of small fixed Pedrail robot with the variable guide wheel angle", *J. Mech. Trans*. **39**(8), 97–110 (2015).
3. S. Pan, L. Shi and S. Guo, "A Kinect-based real-time compressive tracking prototype system for amphibious spherical robots", *Sensors* **15**(4), 8232–8252 (2015).
4. K. X. Ba, Y. H. Song, B. Yu, X. L. He, Z. P. Huang, C. H. Li and X. D. Kong, "Dynamics Compensation of Impedance Based Motion Control for LHDS of Legged Robot", *Robot Auton Syst*, Doi: 10.1016/j.robot.2020.103704 to be published.
5. K. Janne and J. Mattila, "Stability-guaranteed impedance control of hydraulic robotic manipulators", *IEEE/ASME Trans. Mech.* **22**(2), 601–612 (2017).
6. Q. Zhang, Y. Li, T. H. Lee and S. S. Ge, "Neural networks impedance control of robots interacting with environments", *IET Control Theory A*. **7**(11), 1509–1519 (2013).
7. K. X. Ba, G. L. Ma, B. Yu, Z. G. Jin, Z. P. Huang, J. X. Zhang and X. D. Kong, "A nonlinear model-based variable impedance parameters control for position-based impedance control system of hydraulic drive unit", *Int. J. Control Autom. Syst.* **18**(7), 337–344 (2020).
8. F. J. Abu-Dakka, L. Rozo and D. G. Caldwell, "Force-based variable impedance learning for robotic manipulation", *Robot. Auton. Syst.* **109**, 156–167 (2018).
9. W. B. Dong, R. H. Guan, L. T. Yuan and X. L. Gu, "Adaptive Impedance Based Force and Position Control for Pneumatic Compliant System", *43rd Annual Conference of the IEEE Industrial Electronics Society* (2017).
10. M. Kimmel and S. Hirche, "Invariance control for safe human–robot interaction in dynamic environments", *IEEE Trans. Robot.* **33**(6), 1–16 (2017).
11. J. Jun, J. M. Liu and W. H. Chen, "An impedance-based force control scheme to a plate-to-plate nanoimprinter", *IEEE Trans. Nanotech.* **15**(2), 328–336 (2016).
12. M. Souzanchi-K, A. Arab, M. R. Akbarzadeh-T and M. M. Fateh, "Robust impedance control of uncertain mobile manipulators using time-delay compensation", *IEEE Trans. Control Syst. Tech.* **26**(6), 1942–1953 (2017).
13. M. M. Fateh and R. Babaghasabha, "Impedance control of robots using voltage control strategy", *Nonlinear Dyn.* **74**(1), 277–286 (2013).
14. Y. Chen, J. Zhao, J. Wang and D. Li, "Fractional-Order Impedance Control for a Wheel-Legged Robot", *2017 29th Chinese Control And Decision Conference (CCDC)*, Chongqing, China, 28–30 May 2017, pp. 7845–7850.
15. M. M. Fateh and V. Khoshdel, "Voltage-based adaptive impedance force control for a lower-limb rehabilitation robot", *Adv. Robot.* **26**(15), 961–971 (2015).
16. H. Kimura, Y. Fukuoka and A. H. Cohen, "Adaptive dynamic walking of a quadruped robot on natural ground based on biological concepts", *Int. J. Robot. Res.* **22**(5), 187–202 (2003).
17. I. Poulakakis, J. A. Smith and M. Buehler, "Modeling and experiments of untethered quadrupedal running with a bounding gait: The scout II robot", *Int. J. Robot. Res.* **24**(4), 239–256 (2005).
18. J. G. Nichol, S. P. N. Singh, K. J. Waldron and L. Palmer, "System design of a quadrupedal galloping machine", *Int. J. Robot. Res.* **23**(10), 1013–1027 (2004).
19. S. Seok, A. Wang, M. Y. Chuah, D. Otten, J. Lang and S. Kim, "Design Principles for Highly Efficient Quadrupeds and Implementation on the MIT Cheetah Robot", *2013 IEEE International Conference on Robotics and Automation*, Karlsruhe, Germany, 6–10 May 2013, pp. 3307–3312.
20. R. Playter, M. Buehler and M. Raibert, "BigDog", **In**: *Society of Photo-optical Instrumentation Engineers*, Orlando, FL, USA, vol. 6230 (2006).
21. C. Semini, V. Barasuol, T. Boaventura, M. Frigerio, M. Focchi, D.G. Caldwell and J. Buchli, "Towards versatile legged robots through active impedance control", *Int. J. Robot. Res.* **34**(7), 1003–1020 (2015).
22. X. Rong, Y. Li, J. Ruan and B. Li., "Design and simulation for a hydraulic actuated quadruped robot," *J. Mech. Sci. Tech.* **26**(4), 1171–1177 (2012).
23. M. Focchi, V. Barasuol, I. Havoutis, J. Buchli, C. Semini and D.G. Caldwell, "Local Reflex Generation for Obstacle Negotiation in Quadrupedal Locomotion," *Conference on Climbing and Walking Robots (CLAWAR)*, Sydney, Australia, 14–17 July 2013, pp. 443–450.

24. M. Hutter, C. Gehring, M. Bloesch, M. H. Hoepflinger and R. Siegwart, "Starleth: A Compliant Quadrupedal Robot For Fast, Efficient, and Versatile Locomotion," *15th International Conference on Climbing and Walking Robots and the Support Technologies for Mobile Machines*, Baltimore, MD, 23–26 July 2012, pp. 483–490.
25. M. Bajracharya, J. Ma, M. Malchano, A. Perkins and L. Matthies, "High Fidelity Day/Night Stereo Mapping with Vegetation and Negative Obstacle Detection for Vision-in-the-Loop Walking," *IEEE/RSJ International Conference on Intelligent Robots and Systems (IROS)*, Tokyo, Japan, 03–08 November 2013, pp. 3663–3670.
26. T. K. Jin, J. S. Cho, B. Y. Park, S. Park and Y. Lee, "Experimental Investigation on the Design of Leg for a Hydraulic Actuated Quadruped Robot," *IEEE ISR 2013*, Seoul, South Korea, 24–26 October 2013, pp. 1–5.
27. G. Wiedebach, S. Bertrand, T. Wu, L. Fiorio, S. Mccrory, R. Griffin, F. Nori and J. Pratt, "Walking on Partial Footholds Including Line Contacts with the Humanoid Robot Atlas," *2016 IEEE-RAS 16th International Conference on Humanoid Robots (Humanoids)*, Cancun, Mexico, 15–17 November 2016, pp. 1312–1319.
28. G. Tong, J. Gu and W. Xie, "Virtual entity-based rapid prototype for design and simulation of humanoid robots," *Int. J. Adv. Robot. Syst*. **10**(291), 1–9 (2013).
29. X. B. Guo and Q. Song, "Research on modeling and simulation techniques of electromechanical integration based on virtual prototype," *Agro Food Ind. Hi-tech* **28**, 2303–2306 (2017).
30. L. Bi, J. Guo and S. Guo, "Virtual Prototyping Technology-Based Dynamics Analysis for an Amphibious Spherical Robot," *2015 IEEE International Conference on Information and Automation*, Lijiang, China, 8–10 August 2015, pp. 2563–2568.
31. S. Yang and B. Zi, "Design and Analysis of a 2-DOF Hybrid-Driven Planar Parallel Manipulator Based on Virtual Prototype Technology," *2010 2nd International Conference on Signal Processing Systems*, Dalian, China, 5–7 July 2010, pp. 502–506.
32. L. F. P. D. Oliveira and L. R. Flávio, "Modeling, simulation and analysis of locomotion patterns for hexapod robots," *IEEE Latin Am. Trans.* **16**(2), 375–383 (2018).
33. C. A. G. Gutiérrez, J. R. Reséndiz, J. D. M. Santibáñez and G. M. Bobadilla, "A model and simulation of a five-degree-of freedom robotic arm for mechatronic courses," *IEEE Latin Am. Trans.* **12**(2), 78–86 (2014).
34. B. He, L. Han, Y. Wang, S. Huang and L. L. Liu, "Kinematics analysis and numerical simulation of a manipulator based on virtual prototyping," *Int. J. Adv. Manuf. Tech.* **71**(5), 943–963 (2014).
35. H. L. Xie, F. Li, N. Weng and Z. Q. Sheng, "Virtual prototype modeling of biped robot with heterogeneous legs," *Appl. Mech. Mater.* **307**, 117–120 (2013).
36. Z. Lan, Z. Yan and J. J. Xu, "Study of co-simulation of rehabilitation robot for upper limb based on virtual prototype," *Adv. Mater. Res.* **712**(3), 2272–2276 (2013).

Appendix

The servo valve of HDU-2nd in Fig. 1(c) is approximately equivalent to a second-order oscillation link, and the transfer function of the spool position and the input voltage of the servo amplifier is as follows:

$$\frac{X_v}{U_g} = \frac{K_{axv}}{\left(\frac{s^2}{\omega^2} + \frac{2\zeta}{\omega}s + 1\right)} \tag{A.1}$$

Since the pressure loss in the pipeline and valve cavity is much smaller than the throttling pressure loss at the valve port, it can be ignored. Considering the pressure-flow nonlinearity, the oil inlet flow of the servo valve can be expressed as follows:

$$q_1 = K_d x_v \sqrt{\frac{[1 + sgn(x_v)]p_s}{2} + \frac{[-1 + sgn(x_v)]p_o}{2} - sgn(x_v)p_1} \tag{A.2}$$

The return oil flow of servo valve can be expressed as follows:

$$q_2 = K_d x_v \sqrt{\frac{[1 - sgn(x_v)]p_s}{2} + \frac{[-1 - sgn(x_v)]p_o}{2} + sgn(x_v)p_2} \tag{A.3}$$

where convert flow coefficient K_d is as follows:

$$K_d = C_d W \sqrt{\frac{2}{\rho}} \tag{A.4}$$

https://doi.org/10.1017/S0263574720001204 Published online by Cambridge University Press

For asymmetric cylinder hydraulic system, the influence of servo cylinder leakage and oil compressibility are considered, the servo cylinder inlet flow can be expressed as follows:

$$q_1 = A_{p1}\frac{\mathrm{d}\Delta x_p}{\mathrm{d}t} + C_{ip}(p_1 - p_2) + C_{ep}p_1 + \frac{V_1}{\beta_e}\frac{\mathrm{d}p_1}{\mathrm{d}t} \tag{A.5}$$

The return oil flow of the servo cylinder can be expressed as follows:

$$q_1 = A_{p2}\frac{\mathrm{d}\Delta x_p}{\mathrm{d}t} + C_{ip}(p_1 - p_2) + C_{ep}p_2 + \frac{V_2}{\beta_e}\frac{\mathrm{d}p_2}{\mathrm{d}t} \tag{A.6}$$

where x_p is the piston position of the servo cylinder, and the variation of piston position relative to its initial position is as follows:

$$\Delta x_p = x_p - L_0 \tag{A.7}$$

In Eq. (A.5), V_1 is as follows:

$$\begin{aligned} V_1 &= V_{01} + A_{p1}\Delta x_p \\ V_{01} &= V_{g1} + A_{p1}L_0 \end{aligned} \tag{A.8}$$

In Eq. (A.6), V_2 is as follows:

$$V_2 = V_{02} + A_{p2}\Delta x_p \tag{A.9}$$

$$V_{02} = V_{g2} + A_{p2}(L - L_0) \tag{A.10}$$

Considering the influence of load characteristics on the position control system, the force balance equation of the servo cylinder is as follows:

$$A_{p1}p_1 - A_{p2}p_2 = (m_{t1} + m_{t2})\frac{\mathrm{d}\Delta x_p^2}{\mathrm{d}^2\mathrm{t}} + (B_{p1} + B_{p2})\frac{\mathrm{d}\Delta x_p}{\mathrm{d}}t + K\Delta x_p + (F_{f1} + F_{f2}) + F_L \tag{A.11}$$

The transfer function between the feedback voltage of the position sensor and the position of the servo cylinder piston rod is as follows:

$$\frac{U_p}{X_p} = K_X \tag{A.12}$$

Combining with Eqs. (A.1)–(A.12), the block diagram of the position closed-loop control system of HDU-2nd is shown in Fig. 2.

https://doi.org/10.1017/S0263574720001204 Published online by Cambridge University Press